

# Mechanical Measurements of the ALMA Prototype Antennas

A. Greve and J. G. Mangum

**Abstract**—The specifications of the Atacama Large Millimeter Array (ALMA) have placed stringent requirements on the mechanical performance of its antennas. As part of the evaluation process of the VertexRSI and Alcatel EIE Consortium (AEC) ALMA prototype antennas, measurements of the path length, thermal, and azimuth bearing performance were made under a variety of weather conditions and observing modes. The results of mechanical measurements, reported here, are compared to the antenna specifications.

**Index Terms**—Antenna measurements, Radio telescopes.

## I. INTRODUCTION

THE Atacama Large Millimeter Array (ALMA) for astronomical observations at millimeter and sub-millimeter wavelengths (up to the Terra-Hertz region) needs antennas of high mechanical precision and of understandable and predictable behaviour. This behaviour must be established for structural deformations due to gravity, temperature changes, and wind loads. This means, in particular, that a high reflector surface precision, pointing and phase stability must be maintained under all motions of tracking and mapping. We present a summary of tests of the mechanical and thermal behaviour of the 12m diameter VertexRSI and AEC ALMA prototype antennas, built at the VLA site (2000m altitude), New Mexico, USA. The tests were made at several intervals between March 2003 and April 2004, and concentrated primarily on the verification of the antenna specifications, of path length variations and parameters which influence the pointing. The data were also analyzed to understand the general behaviour of the antennas. In the investigation we have paid attention to the fact that variations in the behaviour of the antennas may be predictable or sporadic. We believe that repeatable and/or predictable variations can to a large extent be considered in the pointing model, or any other correction device. The antennas were tested in stationary position, under sidereal tracking, On-the-Fly (OTF) mapping, and in Fast-Switching mode (FSW). A large amount of data was collected during commissioning and thus refer to all types of tracking, OTF, FSW, and unintended 'shaking'.

A more extended summary of these test results was reported by the Antenna Evaluation Group to the National Radio Astronomy Observatory (NRAO) and European Southern Observatory (ESO) (which forms the ALMA partnership) for selection of the ALMA production antenna(s). An overview



Fig. 1. The VertexRSI (left) and AEC (right) ALMA prototype antennas (from [2]).

of these performance results was presented in [2]. The current paper presents a more detailed analysis of the mechanical performance measurements made of the ALMA prototype antennas.

## II. STRUCTURAL DESIGN CHARACTERISTICS

### A. VertexRSI Prototype

The VertexRSI antenna (Figure 1) uses four materials, *i.e.* steel, an Invar cone, low thermal expansion CFRP (carbon fibre reinforced plastic), and CFRP-covered aluminum honeycomb plates. The antenna consists of a triangular pedestal; the azimuth (AZ) bearing; the traverse and the fork arms (the fork); the receiver cabin and Invar cone; the backup structure (BUS); and the quadripod and subreflector. The BUS is made of low thermal-expansion CFRP-plated aluminum honeycomb; the quadripod is made of CFRP; the BUS support cone (on the focus cabin) is made of Invar. The steel focus cabin is thermally controlled and stabilized (Freon system). The pedestal and the fork are made of steel. The steel parts are covered with thermal insulation (foam). The antenna is painted white. The prototype subreflector is made of aluminum, attached by a 50 cm long aluminum tube to the quadripod. The antenna is equipped with gear drives. A modified copy of the ALMA VertexRSI antenna, with special Nasmyth cabins, is the Atacama Pathfinder EXperiment (APEX) telescope located on the Chajnantor site and in operation since 2005. A description of this telescope and its behaviour and results at 460 and 810 GHz are published by [1].

The VertexRSI antenna contains also a metrology system, consisting of two tiltmeters installed in the pedestal; one

Manuscript received May 15, 2006; revised August 17, 2007.

The performance results presented in this publication were part of a comprehensive technical evaluation process used to evaluate the ALMA prototype antennas which concluded in April 2005.

tiltmeter above the AZ bearing; and one tilmeter at each elevation bearing. An independent CFRP reference frame is mounted inside the fork. This reference structure supports, at each elevation bearing, two linear displacement sensors, of which the output difference is expected to be a measure of the tilt of the antenna in the direction perpendicular to the elevation axis. We have analyzed the tilmeter readings; however, we have not tested the functionality of the metrology system.

In order to obtain data on the temperature distribution within the VertexRSI antenna, 89 temperature sensors, distributed throughout the pedestal, the fork, the BUS, and the quadripod and subreflector, were installed at customer's request. The sensors do not form a part of the metrology system. It is found that the measurements are useful for the understanding, or even prediction, of the thermal state of the antenna, and for prediction of temperature induced path length variations of the steel parts.

### B. AEC Prototype

The AEC antenna (Figure 1) uses two materials, i.e. steel and CFRP. The AEC antenna consists of a cylindrical double-walled steel base (the external and internal pedestal), the AZ bearing, the traverse and the fork arms (the fork), the receiver cabin, the backup structure (BUS), the quadripod and the subreflector. The receiver cabin, the BUS and the quadripod are made of low thermal-expansion CFRP plates. The other parts are made of steel. The steel parts are covered with thermal insulation (foam). The antenna is painted white. The prototype subreflector is made of aluminum, attached by a 50 cm long aluminum tube to the quadripod. The antenna is equipped with linear drives.

The AEC antenna contained initially a metrology system consisting of Automated Precision Incorporated 5D devices (see §IV), installed in both fork arms. The metrology system was not put into operation, and has not been tested. The AEC antenna contains 101 temperature sensors, distributed throughout the pedestal and the fork. These sensors were initially part of the metrology system; they have not been tested for this purpose.

A picture of the AEC prototype antenna can be found in [2].

### III. SCOPE OF THE TESTS

The aim of the tests was the verification of mechanical specifications, laid down in the "ALMA Project Statement of Work". This paper presents measurements, and their analysis, of

- Path Length Variations,
- Thermal Behaviour,
- AZ Bearing Precision.

These tests were performed under a variety of motions of the antenna (stationary, slewing, tracking, OTF, and FSW observations) and meteorological conditions (stable conditions, ambient air temperature variations, variations of wind speed and angle of attack of the wind, different solar illumination). While the conditions of telescope motion were, to a large

TABLE I  
APPLICATION OF INSTRUMENTATION

Instrument	Application	Antenna
<b>QD</b>	Deformation Measurements: Gravity Deformation BUS	AEC
<b>API</b>	Path-Lengths: Pedestal ( $L_1$ ) Fork Arm ( $L_2$ ) Vertex to Subreflector ( $L_3$ )	VertexRSI VertexRSI, AEC VertexRSI, AEC
<b>T-Sensors</b>	Temperature Behaviour: Pedestal Traverse Fork Arms Receiver Cabin Invar Cone BUS Quadripod & Subreflector	VertexRSI, AEC VertexRSI, AEC VertexRSI, AEC VertexRSI VertexRSI VertexRSI VertexRSI
<b>Tiltmeter</b>	Tilt Measurements: AZ Axis	VertexRSI, AEC

extent, controllable, the meteorological conditions obviously were not. This concerns in particular the wind conditions.

Measurements, made during the AEG test time, of gravity induced deformations of the VertexRSI antenna BUS were not successful since the supplied laser mount inside the reflector vertex hole was unstable against tilt. However, on the VertexRSI antenna the change of the subreflector distance as function of elevation has been determined since these measurements are not affected by a tilt of the mount. Gravity induced deformations were measured on the AEC antenna which had a stable mount inside the reflector vertex hole, used earlier for laser tracker surface measurements. On this antenna the change of the subreflector distance as function of elevation has been determined, as well as gravity deformations of the rim of the BUS.

### IV. EMPLOYED INSTRUMENTATION

The instrumentation employed for the tests, listed in Table I, consisted of:

- A Laser-Diode Quadrant Detector (QD) [produced by FixturLaser (Sweden)]; able to measure deviations (x,y) perpendicular to the laser beam;
- API 5D Measurement Device (API) [produced by Automated Precision Incorporated (USA)], able to measure relative changes in distance ( $\Delta z$ , laser interferometer), deviations (x,y) perpendicular to the laser beam, and perpendicular tilts of the target;
- PT 100 Temperature Sensors [manufactured by TC Group (USA)]; of 0.1 to 0.3° C precision;
- Tiltmeters [manufactured by Applied Geomechanics (USA)], of 0.1 arcsec precision.

### V. PATH LENGTH MEASUREMENTS

The path length specification for the ALMA prototype antenna states that *the antenna should have a non-repeatable/repeatable path length variation  $\leq 15/20\mu\text{m}$ , respectively, within the time between expected consecutive calibrations of the interferometer array (15–30 minutes).*

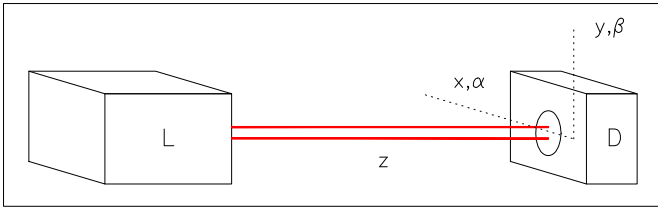


Fig. 2. Schematic of the API 5 D measurement equipment. The instrument measures the variation of the distance  $z$ , the position shift  $x, y$ , and the rotation  $\alpha, \beta$  around the axes  $x, y$ . L = laser beam emitter and fringe counter, D = detector (target).

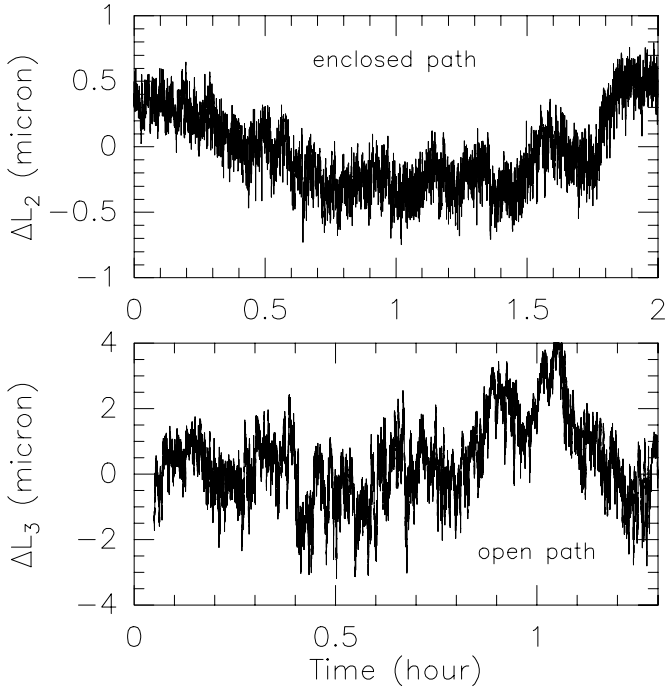


Fig. 3. API measurement of path length changes ( $\Delta z$ ) inside the fork arm (enclosed path) and toward the subreflector (open path).

The API5D and QD measure straightness variations of a laser beam perpendicular to the line-of-sight. The measurements are mainly affected by atmospheric turbulence, of approximately 0.5 arcsec (rms) in both directions. The accuracy of open-air or enclosed measurements over typical distances of the antenna size is  $\sim 5 \mu\text{m}$ .

The path lengths were measured with the API Laser Interferometer. As illustrated in Fig. 2, as one particular option the API measures path length variation in the line-of-sight by laser interferometry. The accuracy of the measurements ( $\Delta z$ ) is better than  $1 \mu\text{m}$  for an enclosed path, and 2 to  $3 \mu\text{m}$  micron for an open-air path, as illustrated in Fig. 3.

With the API instrument it is not possible to measure the full path length variation between, for instance, the receiver and the ground (foundation), thus evaluating the integrated behaviour of the antenna as it affects the phase of the interferometer array. The path length variations of several individual structural sections were measured instead, with the understanding that the full path length variation is approximately the sum of the components (see Tables II). As shown in Fig. 4, these measurements contain

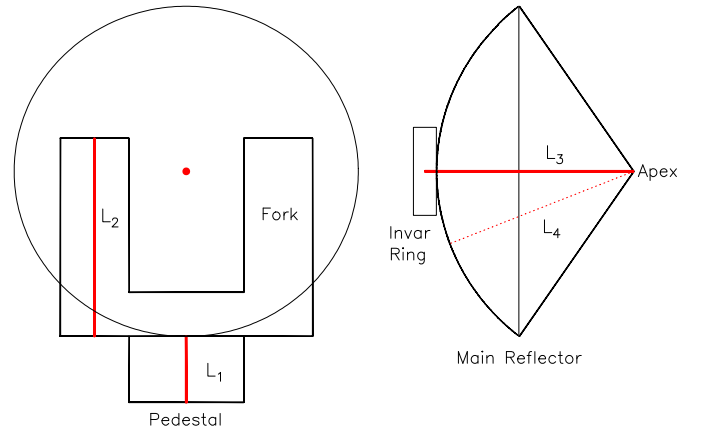


Fig. 4. Illustration of the Path Length measurements  $L_1$ ,  $L_2$ ,  $L_3$ , and  $L_4$  (from [2]).

- L1: path length inside the pedestal = distance between the foundation (ground) and the lower face of the azimuth (AZ)-bearing; it was not possible to measure this path length on the AEC antenna;
- L2: path length inside (one) fork arm (left, right) = distance between the lower part of the traverse and the upper part of the left (right) fork arm, below the elevation (EL)- bearing;
- L3: path length along the radio axis = distance between the upper part of the Invar cone (VertexRSI), or the vertex hole (AEC, laser tracker mount) of the main reflector, and the apex of the subreflector; (in the measurements the dilatation of the aluminum subreflector support tube (50 cm length) has been eliminated, as far as possible; see §V-C);
- L4: path length of the reflector = distance between the Invar cone/vertex hole and a point of the reflector surface, measured via the subreflector. On both antennas this path length measurement was tested but not routinely performed, mainly because of difficult installation and alignment, and time limitations. Since, in essence, this path length component is the CFRP part of the antennas, at least a temperature induced path length variation is expected to be small.

#### A. Summary of Path Length Variations

From simple geometrical and material arguments (thermal expansion coefficients), and the fact that wind forces act on short time scales, it was evident from the beginning that the path length changes are, primarily, due to thermal dilatation of the antenna components, induced by variation of the ambient air temperature and solar radiation, buffered by the surface finish (paint) and thermal insulation. In the analysis of path length variations we have therefore selected time intervals ( $\Delta t$ ) of 3 minutes, comparable to the time scale of wind, of 10 minutes, comparable to FSW and OTF modes of observation, and of 30 minutes, comparable to the time between upgrades of the pointing and interferometer phases. The corresponding path length measurements of the VertexRSI and the AEC antenna, as function of time of the day (local time = UT -

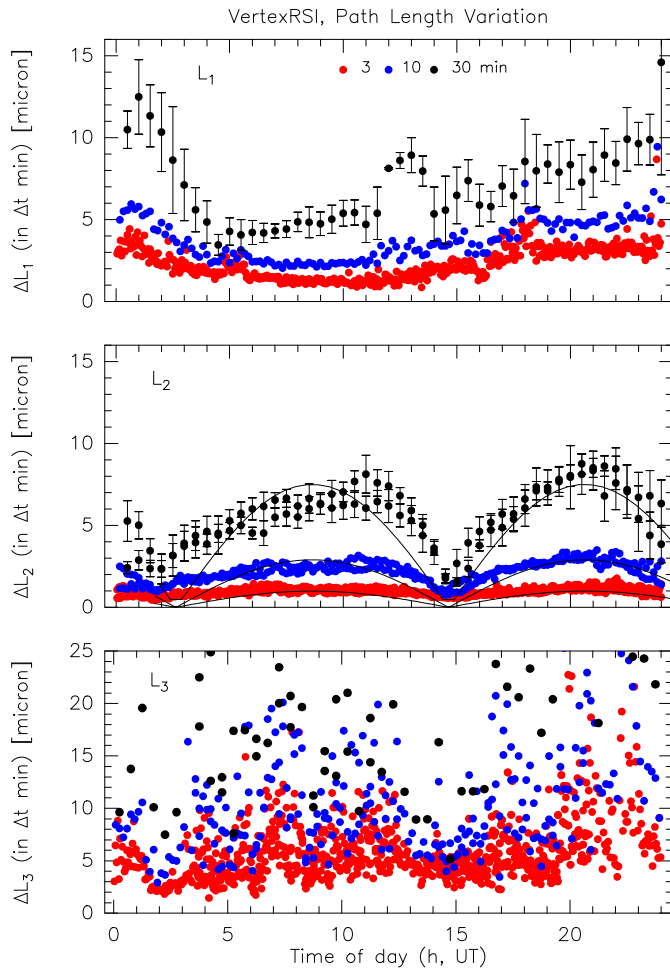


Fig. 5. VertexRSI antenna. Daily variation of path length L1: pedestal, of path length L2: fork arm, and of path length L3: Invar cone to subreflector, as function of the time of the day (UT), and within time intervals of 3, 10, and 30 minutes duration. The lines in the  $\Delta L_2$  panel are explained in §V-C (from [2]).

7h), are shown in Fig. 5 and 6. The results are summarized in Table II. The data shown in Fig. 5 and 6 were obtained during long time periods (see Table II), and cover a large variety of antenna motions. For path lengths which could not be measured an estimated value is entered in the tables.

### B. Path Length Variations Influenced by Temperature and Wind

In order to understand the origin of the path length variations, and for purposes of predictions, we have searched for correlation of the path length changes with the steel temperature of the pedestal and the fork, the ambient air temperature, and the wind speed. The correlation of the fork arm path length change  $\Delta L_2$  is shown for the VertexRSI antenna in Fig. 7, and for the AEC antenna in Fig. 8. As to be expected, the correlation of the path length change  $\Delta L_2$  with the change of the fork steel temperature is good, and usable for prediction. On the VertexRSI antenna, a similarly useful correlation was found for the path length of the pedestal ( $L_1$ ). Also as expected, there is no significant correlation between

TABLE II  
PATH LENGTH VARIATIONS

Path	VertexRSI <sup>a</sup> ( $\mu\text{m}, \mu\text{m}, \mu\text{m}, \text{hr}$ )	AEC <sup>a</sup> ( $\mu\text{m}, \mu\text{m}, \mu\text{m}, \text{hr}$ )
L <sub>1</sub> : pedestal	3/6/10/250	$\sim 5/\sim 5/\sim 5/\text{est}$
L <sub>2</sub> : fork arm	1.5/3/8/360	3/4/10/360
L <sub>3</sub> : quadripod	5/5/5/25	4/5/ $\sim 10$ /25
L <sub>4</sub> : reflector	$\sim 5/\sim 7/\sim 9/\text{est}$	$\sim 5/\sim 5/\sim 5/\text{est}$
$\Delta z$	15/21/32/635	15/18/30/385

<sup>a</sup> Each measurement listed as averages over 3, 10, and 30 minute durations, along with the total measurement time (or estimate), for each path.

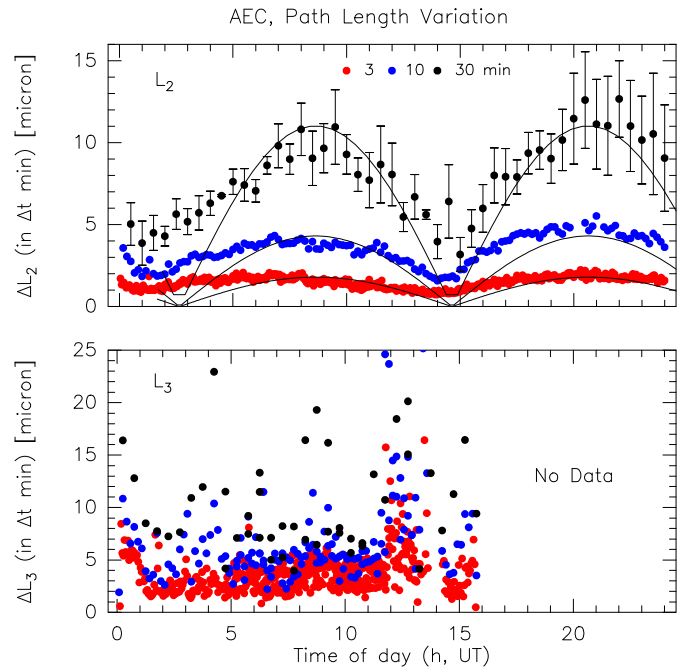


Fig. 6. AEC antenna. Daily variation of path length L2: fork arm, and of path length L3: vertex platform to subreflector, as function of the time of the day (UT), and within intervals of 3, 10, and 30 minutes duration. The lines in the  $\Delta L_2$  panel are explained in §V-C (from [2]).

path length variation and ambient air temperature or wind speed variation.

A dedicated investigation of path length changes with wind speed was difficult because of timing. For one particular day, with changes of the wind speed ( $v$ ) from  $\sim 5$  m/s to  $\sim 15$  m/s, the path length variation  $\Delta L_2$  (fork) of the VertexRSI antenna is shown in Fig. 9. The data seem to indicate an increase of  $\Delta L_2$  with an increase of the wind speed. However, the measured variation of  $L_2$  is tolerable even for the specified highest wind speed of observation with the interferometer array, of  $v = 9$  m/s. There are no data for the AEC antenna.

During the measurements shown in Figure 9 a gradual change of the fork temperature occurred as well which produced a drift of  $L_2$  with time. This effect is not considered in the construction of Figure 9. A detailed view of the wind speed and the path length variation  $\Delta L_2$  with a linear temperature induced drift of  $L_2$  removed is shown in Figure 10. It is seen that the path length  $\Delta L_2$  hardly changes by  $\pm 2 \mu\text{m}$  although the gusty wind changes velocity between 5 and 20 m/s. The path length  $L_2$  is insensitive to the gusts of the

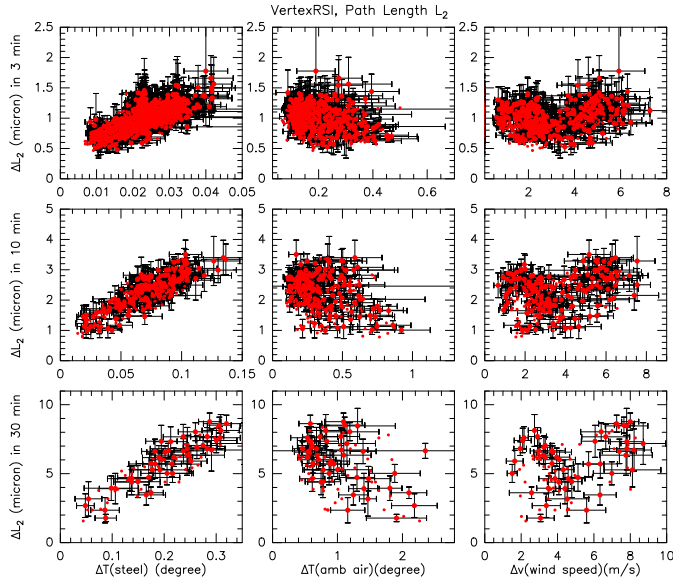


Fig. 7. VertexRSI antenna. Dependence of  $\Delta L_2$  on the temperature variation of the fork,  $\Delta T(\text{steel})$ , on the temperature variation of the ambient air,  $\Delta T(\text{amb air})$ , and the variation of the wind speed,  $\Delta v$  (from [2]).

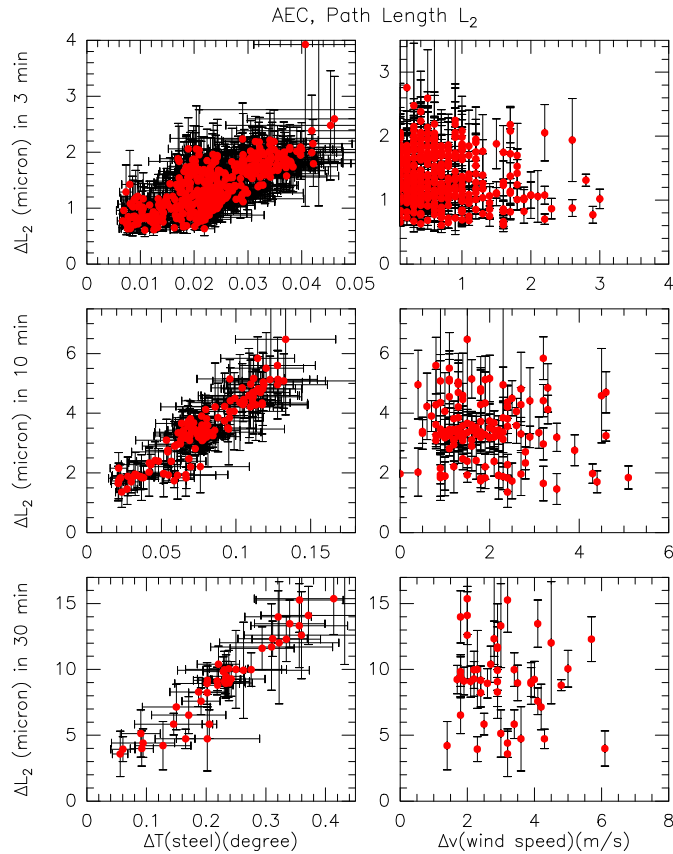


Fig. 8. AEC antenna. Dependence of  $\Delta L_2$  on the temperature variation of the fork,  $\Delta T(\text{steel})$  and the variation of the wind speed,  $\Delta v$ . Measurements of the ambient air temperature were not available (from [2]).

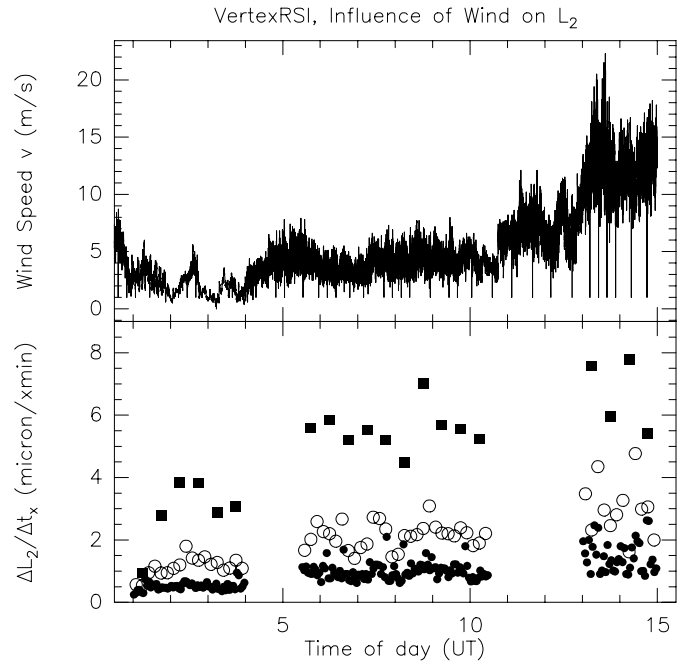


Fig. 9. VertexRSI antenna. Correlation of path length variation  $\Delta L_2$  with wind speed for 3 (dots), 10 (open circles), and 30 (squares) minute intervals.

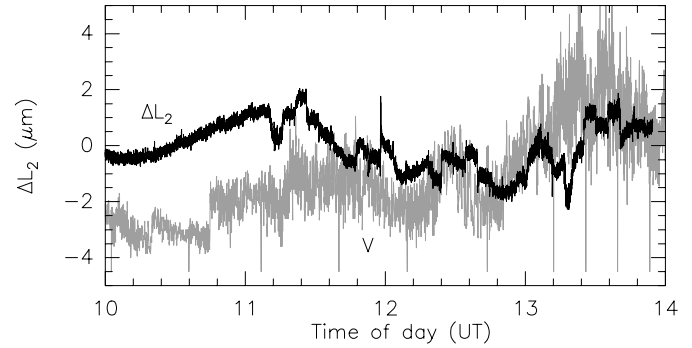


Fig. 10. VertexRSI antenna. Correlation of path length variation  $\Delta L_2$  (bold line) with wind speed for  $v_{\text{wind}} = 0\text{--}20$  m/s for a typical four hour observation period.

wind. The apparent increase in path length variation  $\Delta L_2$  with wind speed, shown in Figure 9, is probably due to a faster temperature change of the fork at higher wind speed (convective cooling) than a mechanical effect of the wind.

### C. Influence of Material Thermal Properties on L<sub>3</sub>

On both antennas, the prototype subreflector was connected to the quadripod by a 50 cm long aluminum tube. The large thermal dilatation of this tube ( $\sim 25 \mu\text{m}/\text{m}/\text{K}$ ), due to some extent to the asymmetric influence of the ambient air (wind) and due to asymmetric solar radiation, disturbed the path length measurements of L<sub>3</sub>. However, as shown in Fig. 11, the measurements were corrected for this effect, as well as possible. The large scatter of  $\Delta L_3$  in Figs. 5 and 6 is due, to some extent, to an asymmetric influence of the ambient air temperature (wind) and due to asymmetric solar illumination. However, on the final antennas the use of aluminum should

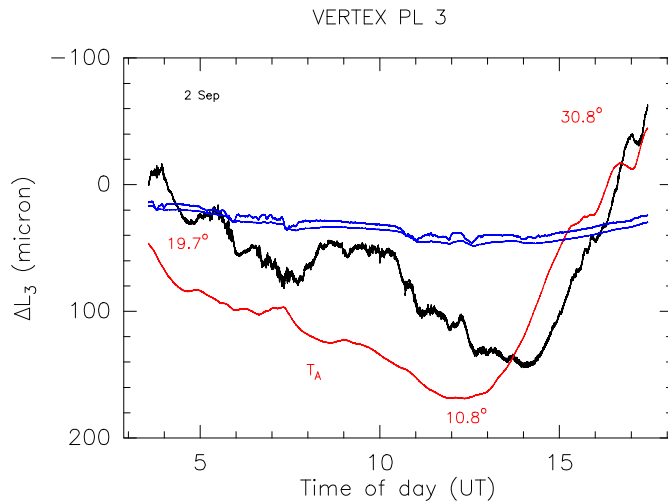


Fig. 11. VertexRSI antenna. Measured path length variation  $\Delta L_3$ : black line; measured ambient air temperature:  $T_A$ ; the air temperature at the beginning and the end of the measurement is given in the figure; temperature of the quadripod near the subreflector: parallel lines (same scale of the temperatures).

be avoided for essential structural parts which affect the path length. The measurement on the AEC antenna is similar.

#### D. Path Length Predictions from Steel Temperature Measurements

Both antennas have temperature sensors installed on the steel walls inside the fork arms. From these recordings we have derived the average temperature of each fork arm, and the maximum and minimum temperature, as shown in Fig. 12. The measured temperature distribution was used in the finite element models (FEM) of the fork arms to calculate the corresponding thermal dilatation  $\Delta L_2$ . Comparing the calculated thermal dilatation with the path length variation measured directly with the API, we find very good agreement as shown in Fig. 12. From this we conclude that the path length variations of the steel parts can be predicted, to a high degree of accuracy, from representative temperature measurements used in the finite element model, or an empirical relation. The final number of temperature sensors of the pedestal and the fork arms can, however, be reduced to 3 or 4, per component.

The daily temperature variation of the fork arms and the corresponding path length variation  $\Delta L_2$ , both shown in Fig. 12, can be approximated with good accuracy by sine-functions. This holds also for the ambient air temperature, at least as measured at the VLA site during most of the time of the tests. When adopting a sine-function  $L_2(t) = L_0 + \Delta L_2 \sin(\omega t)$ , with  $\omega = 2\pi/24\text{h}$  and  $t = \text{time}$ , the path length variation  $\Delta L_2$  at a 3, 10, and 30 minute time interval can be derived by differentiation of the function  $L_2(t)$ . The smallest variation of  $L_2(t)$  occurs around the temperature minimum and maximum of the ambient air ( $T_A$ ) and of the fork steel ( $T_F$ ). From weather data at the site and temperature measurements we find that  $T_F \simeq T_A + 3\text{h}$ . As evident from Fig. 12, the maxima and minima of the fork arm temperature (and the ambient air temperature) occur around 0h and 15h UT (7h and 17h local time) but not late at night or at noon.

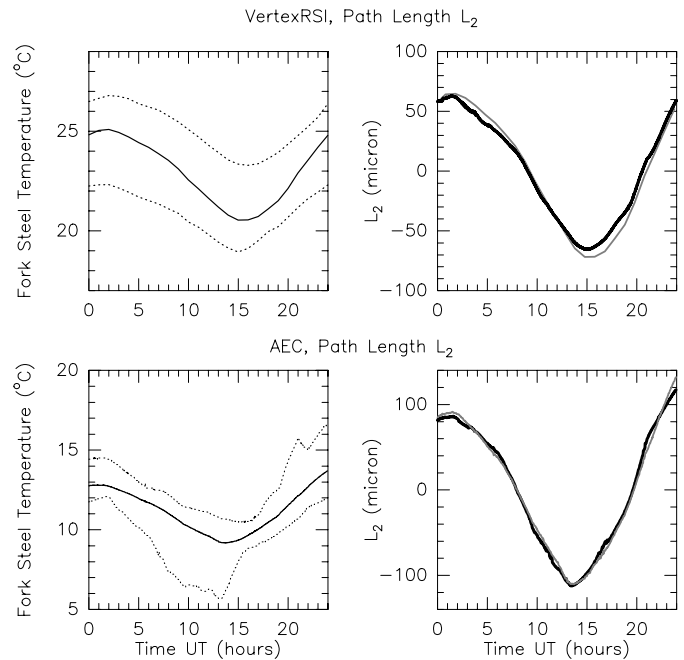


Fig. 12. VertexRSI antenna and AEC antenna. Agreement between the path length variation  $\Delta L_2$  measured with the API laser interferometer and FEM-calculated from the measured temperatures (14 sensors). (a) average temperature of the fork arm steel derived from 14 sensors: solid line, maximum and minimum fork arm steel temperature: dashed lines. (b) measured path length variation: black line, path length variation calculated from the FEM using the average temperature: grey line. Similar results for other days (from [2]).

The result of the differentiation of  $L_2(t)$  is shown by solid lines in Fig. 5 and 6, which gives an explanation of the double peaked form of the measured variations. The minima of  $\Delta L_2$  occur around sunrise (around 7h local) and sunset (around 17h local) where the temperatures go through maximum and minimum and show the smallest change with time.

As evident from Fig. 12, the total daily path length variation of the fork arms is of the order of  $100\ \mu\text{m}$  to  $200\ \mu\text{m}$ , as fully understandable, and unavoidable, from the height of the fork arms, the thermal properties of steel, the actual temperature variation of the steel, and the solar illumination. The relevant information for operation of the interferometer array is however contained in the values for the 3, 10, and 30 minute time intervals.

#### E. Path Length Variations During Antenna Motion

The ALMA interferometer will use sidereal tracking, OTF mapping, and FSW motions between source and calibrator. The OTF, and in particular the FSW motions, involve high accelerations of the antenna which may affect the path length stability. The path length variations  $\Delta L_1$ ,  $\Delta L_2$  and  $\Delta L_3$  were measured under the following motions of the antennas: (1) sidereal tracking, as a combined motion in AZ and EL direction; (2) OTF motion of  $1^\circ$  AZ by  $1^\circ$  EL, at  $0.05^\circ/\text{s}$ ; and (3) FSW motion of  $1^\circ$  AZ by  $1^\circ$  EL, at  $6^\circ/\text{s}$  in AZ and  $3^\circ/\text{s}$  in EL.

For both antennas, the variations of the path lengths  $L_1$ ,  $L_2$ , and  $L_3$  are within  $\pm 2\ \mu\text{m}$  for sidereal tracking and OTF motion. For FSW motion, with the highest acceleration at

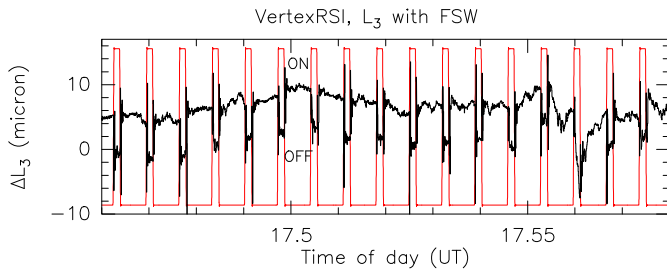


Fig. 13. VertexRSI antenna. Path length variation  $\Delta L_3$  (Invar cone to subreflector) during Fast-Switching motion. The switching cycle is shown by the step line, the path length changes by the black line. The ON (10s) and OFF (2s) position is indicated (from [2]).

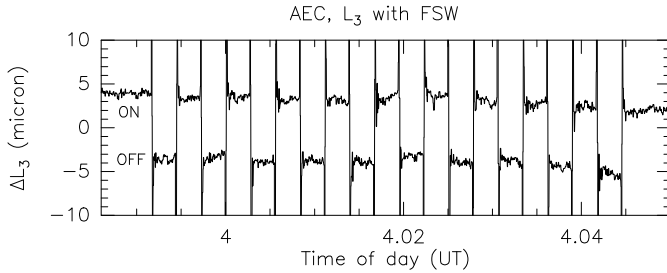


Fig. 14. AEC antenna. Path length variation  $\Delta L_3$  (reflector vertex hole to subreflector) during Fast-Switching motion. The ON (10s) and OFF (10s) position is indicated (from [2]).

the subreflector position of the quadripod, the path length measurements  $L_3$  are shown in Fig. 13 and 14. Again, for both antennas the path length variation  $\Delta L_3$  at the ON and OFF position is within  $\pm 3 \mu\text{m}$ .

#### F. Influence of Gravity on $L_3$

Because of gravity induced deformations, on both antennas the path length  $L_3$  will change with elevation of the reflector. The major part of this change is due to the influence of gravity, and is predictable and repeatable. To measure this effect, the laser emitter of the API was installed on a mount (especially constructed for the VertexRSI antenna; the laser tracker platform on the AEC antenna) at the reflector vertex, the retro-reflector was installed on the subreflector. The measurements of the  $L_3$  path length variation as function of elevation are reliable because the measurements are insensitive to a small tilt of the laser mount relative to the antenna structure, and hence of the laser beam reflected in the retro-reflector. The antennas were tipped in elevation (E) in steps of  $15^\circ$ , between  $15(5)^\circ$  and  $90^\circ$  elevation, and the variation of  $\Delta L_3(E)$  was recorded, as shown in Fig. 15 and 16. This path length variation as predicted from a FEM calculation is inserted in the figures. Note in Fig. 15 that the change in subreflector position as measured by photogrammetry (GSI, November 2002) agrees well with the API measurement.

#### G. Gravitational Deformation of the AEC BUS

Any gravity-induced deformation of the main reflector has an influence on the path length ( $L_4$ ), although it can be corrected for since the deformation can be calculated from the FEM. Because of the stable laser tracker mount installed

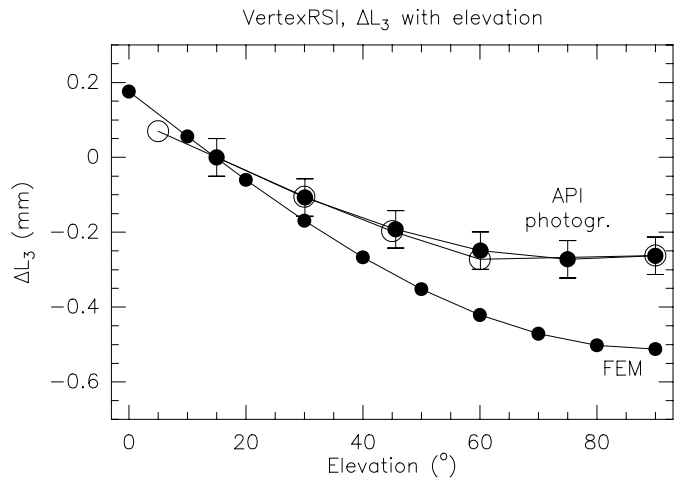


Fig. 15. VertexRSI antenna. Path length variation  $\Delta L_3$  as function of elevation of the reflector, measured with the API (dots) and by photogrammetry (open circles). The curve indicated FEM is the calculated variation (from [2]).

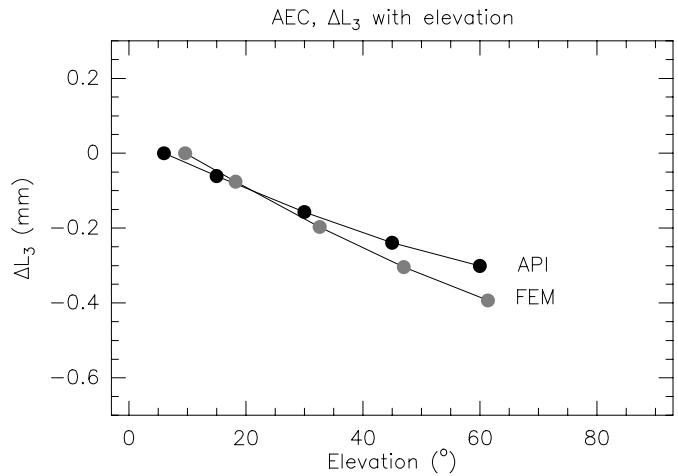


Fig. 16. AEC antenna. Path length variation  $\Delta L_3$  measured (API) as a function of elevation of the reflector. The curve indicated FEM is the calculated variation (from [2]).

on the AEC antenna, a deflection measurement of the reflector rim was made with the QD. The laser emitter was installed on the mount at the reflector vertex, the detector was installed consecutively at several positions on the reflector rim (lower section). The deviation of the laser beam on the detector was measured while the reflector was tipped in elevation. The result of the measurement is shown in Fig. 17 together with the prediction of the FEM calculation.

#### H. The API5D System as a Metrology Device

The full five-dimensional capacity of the API5D system has been used to measure the displacements ( $\Delta x, \Delta y$ ) and the tilts ( $\Delta \alpha, \Delta \beta$ ) of a location close to the elevation bearing(s), and to use this information for the elevation axis pointing error (nodding error). On the VertexRSI antenna a few API5D recordings were made (while using the  $\Delta z$  information) with the laser emitter placed on the transverse of the fork and the detector installed just below the elevation bearing (see Fig. 4,  $L_2$ ). The orientation of the  $(x, y, \alpha, \beta)$  axes and rotations

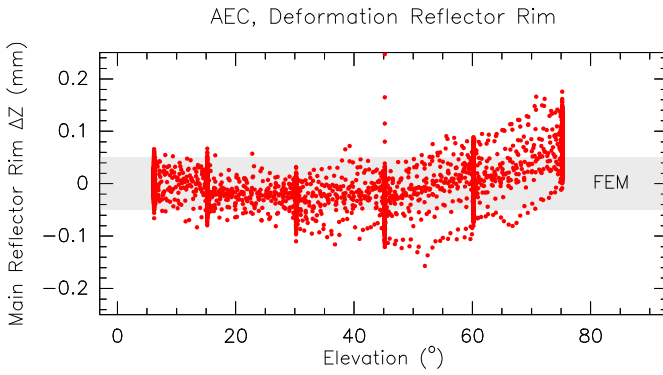


Fig. 17. AEC antenna. Measured deformations of the reflector rim, lower half of the reflector. The antenna was halted at the elevations 5, 15, 30, 45, 60, and 75 degrees. The FEM calculation predicts values within the indicated gray band.

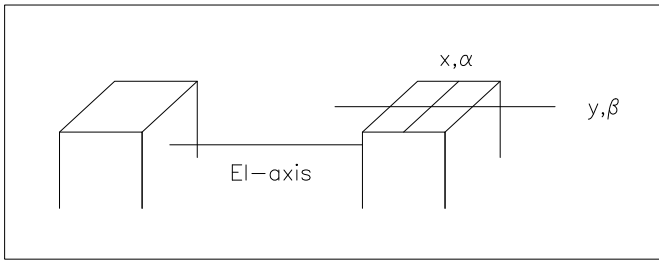


Fig. 18. Orientation of the displacement directions ( $x, y$ ) and the tilt directions ( $\alpha, \beta$ ) for the full API5D measurements of the fork arm structure.

are shown in Fig. 18, the recordings of  $(\Delta x, \Delta y, \Delta \alpha, \Delta \beta)$  during several days are shown in Fig. 19. A rather regular daily excursion is seen, of the order of  $(\Delta x, \Delta y, \Delta \alpha, \Delta \beta) \simeq (\pm 100 \mu\text{m}, \pm 200 \mu\text{m}, \pm 5 \text{arcsec}, \pm 15 \text{arcsec})$ . For a length of the fork arm of  $L_2 \simeq 3\text{m}$ , it is found that  $\Delta x' \simeq L_2 \Delta \alpha \simeq 70 \mu\text{m}$  and  $\Delta y' \simeq L_2 \Delta \beta \simeq 200 \mu\text{m}$ , apparently in agreement with the measured values  $(\Delta x, \Delta y)$ . This agreement also indicates that the  $(\Delta \alpha, \Delta \beta)$  data are probably not independent.

While it is plausible that the measured effect is due to temperature variations, the FEM calculations using the measured temperatures of the fork arm (see Fig. 12) yielded dilatations and rotations of the steel plates which did not match the measurement. The measured behaviour is also not seen in the pointing model. Our result may be in the same line of similar difficulties encountered in temperature and inclinometer measurements made on larger alidade structures [13].

Since the data of Figure 19 show a clear repeatability, over several days, it still is worthwhile to pursue an interpretation since it may open the possibility to measure pointing changes along the elevation axis and perpendicular to the elevation axis (nodding error). The higher stability of the API system may be of advantage with respect to inclinometers often having drifts.

## VI. THERMAL BEHAVIOUR

### A. Distribution of Temperature Sensors

An investigation of the thermal homogeneity of the antennas gives insight into the expected deformation of these structures.

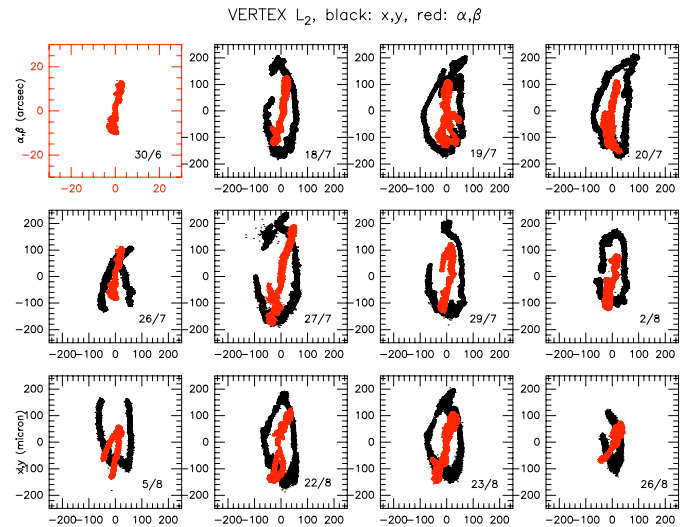


Fig. 19. Measured displacements  $(\Delta x, \Delta y)$  (black) and tilts  $(\Delta \alpha, \Delta \beta)$  (gray) for several days as indicated.

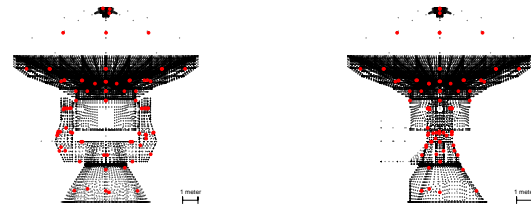


Fig. 20. VertexRSI antenna. Distribution of temperature sensors (big dots). The small dots are nodes of the FEM.

The VertexRSI antenna is equipped with 89 PT-100 temperature sensors (Fig. 20). The steel components of the antenna (pedestal, fork) are insulated, while the steel focus cabin is in addition temperature controlled. The BUS is supported on an Invar cone; the BUS and the quadripod are made of honeycomb-CFRP plates and CFRP. The pedestal and the fork of the AEC antenna are equipped with 101 sensors (Fig. 21). The pedestal and fork is insulated. The focus cabin, BUS, and quadripod are made of CFRP, and were not fitted with thermal sensors due to the low coefficient of thermal expansion of these components.

On the VertexRSI antenna the temperature sensors were regularly placed to represent approximately equal volume elements of the structure. On the AEC antenna, the temperature sensors were part of the metrology system, though not tested in this function. Using the FEM in the way described by [4], AEC antenna temperature sensors were placed to give optimal information about the temperature-induced pointing errors from the fork arm supports.

### B. Measured Temperatures

For example, Fig. 22 shows a representative diurnal temperature distribution measured throughout the VertexRSI antenna. For the day shown, we unfortunately have no measurements of the solar illumination. It was a clear day and the antenna parked in a stationary position looking towards the southern

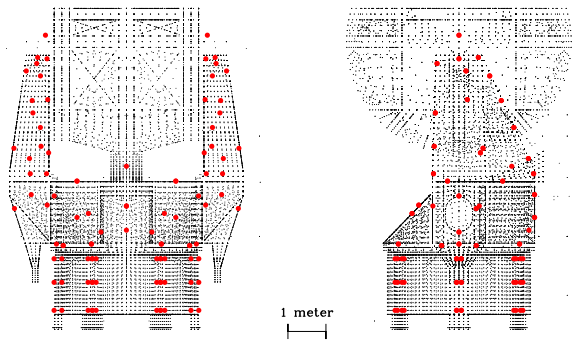


Fig. 21. AEC antenna. Distribution of temperature sensors (big dots). The small dots are nodes of the FEM.

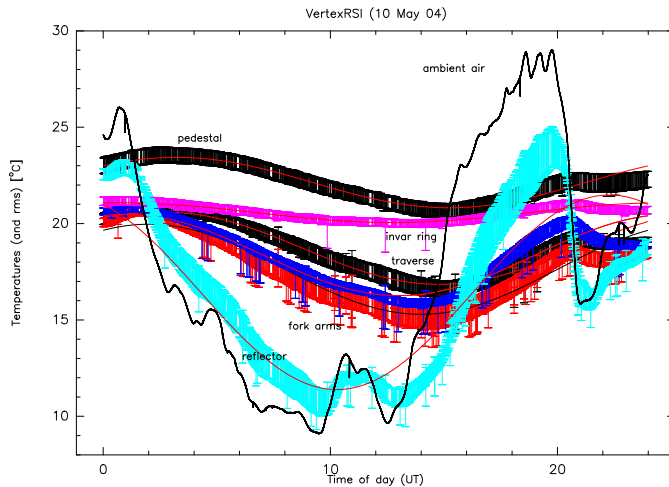


Fig. 22. Measured temperatures of the VertexRSI antenna, for individual components as indicated. The width of the lines is the rms-value of the temperature throughout the indicated component. Sinusoidal fits are shown in red. Very similar temperature distributions were measured on other days during the same season.

horizon. We note that the temperature variation of the pedestal, the traverse, and the fork arms are small. Also, the temperature variation, and the rms value, of the Invar cone, as found for this day and other days, is quite small. The Invar cone is the ventilated upper ring of the focus cabin, which itself is stabilized in temperature by active thermal control. The Invar cone supports the BUS, and hence no print-through of thermal deformations is expected to occur. The BUS itself shows a large daily temperature variation, similar to that of the ambient air. However, the rms-deviation of the temperature is small, of the order of  $3^\circ\text{C}$ . A small differential thermal deformation of the BUS is expected to occur, though being rather harmless, since the BUS consists of 24 independent sectors, with each sector containing several smaller compartments.

Fig. 23 shows, for the same day, the temperature distribution measured on the AEC antenna. The temperatures of the components are very similar, while also the temperature variations are very small.

The sensors of the VertexRSI antenna allow the measurement of the temperature distribution throughout the BUS (Fig. 20). From the measurement of 26 sections of the BUS we determined the average temperature, i.e.  $T_B$ , and deviations

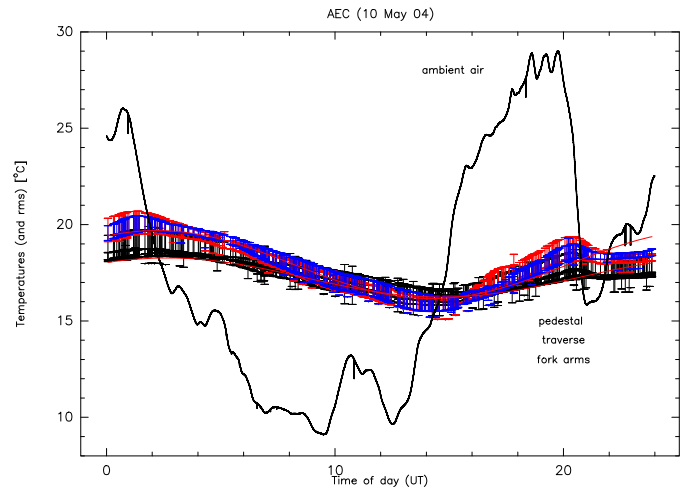


Fig. 23. Measured temperatures of the AEC antenna, for individual components as indicated. The width of the lines is the rms-value of the temperature throughout the indicated component. Sinusoidal fits are shown in red. Very similar temperature distributions were measured on other days during the same season.

from the average  $\Delta T_i = T_i - T_B$ , with  $i = 1, \dots, 26$ . The values  $\Delta T_i$  determine the degree of thermal homogeneity and the residual thermal deformation of the BUS. A representative temperature recording is shown in Fig. 24.

The BUS of the VertexRSI antenna is made of CFRP-plated Al-honeycomb plates, while the BUS of the AEC antenna is made of CFRP plates. The thermal behaviour of both BUS constructions is expected to be comparable. However, the support of the BUS is different. The BUS of the VertexRSI antenna is supported on a temperature stabilized Invar ring, while the BUS of the AEC antenna is supported on a CFRP support structure. The temperature homogeneity of the Invar ring, expressed as the rms value of the temperature distribution, is shown in Figure 25, derived from measurements of four consecutive days. The rms value is  $\sim 0.25\text{C}$  all the time. The BUS rests on a stable support.

### C. VertexRSI Antenna: Influence of Direct Solar Radiation

The ALMA antennas may be used for observations of the Sun, or observations very close to the Sun. A temperature measurement of the VertexRSI antenna tracking the Sun was made on 13 Jul 2003. The comparison of the temperature distribution of the 26 BUS elements for a normal day (Fig. 24) and the Sun tracking condition is shown in Fig. 26. This figure illustrates that there is no noticeable distinction in the temperature variation across the BUS for an observation which tracks the Sun, as requested in the antenna specifications.

### D. Thermal Response of Antenna Components

From the continuously monitored temperatures  $T_i$  of the antenna components [i] and the ambient air temperature  $T_A$  we determined the thermal response  $\beta_i$  using the relation  $\Delta T_i = \beta_i \Delta T_A$ , with  $\Delta T_i$  and  $\Delta T_A$  the daily amplitude of the respective temperature. This relation neglects the influence of direct solar radiation, however, the antennas were randomly observing the sky. For a time of  $\sim 14$  days, the values  $\beta_i$  in

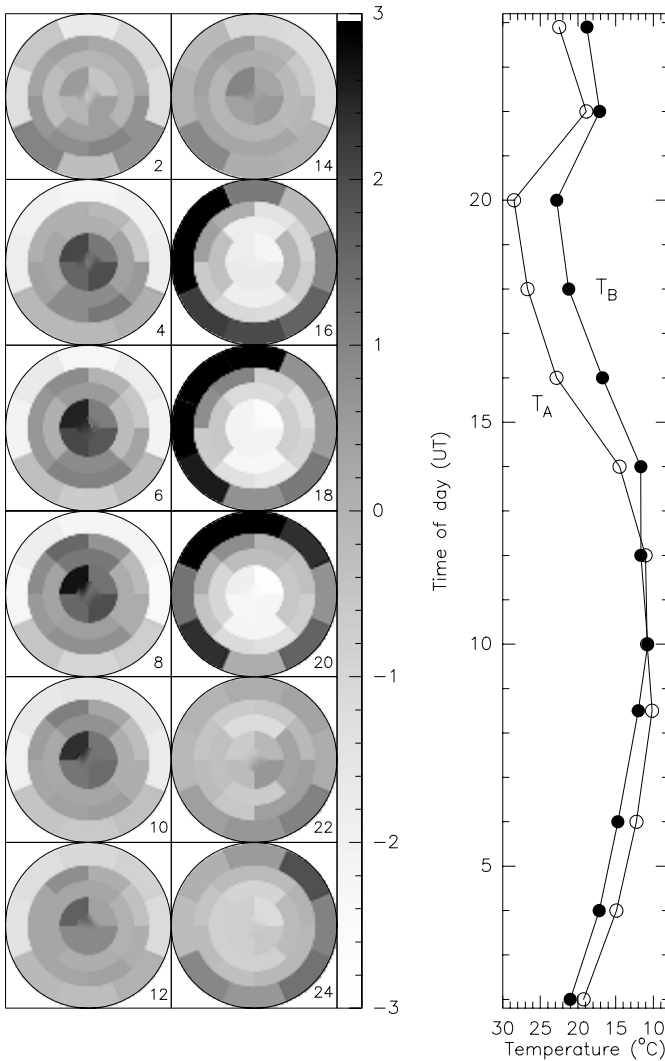


Fig. 24. VertexRSI antenna. Temperature distribution of the 26 BUS elements monitored with sensors; stationary antenna. The left panel shows the deviations from the instantaneous average temperature of the BUS. The wedge indicates temperature in degree C. The right panel shows the average temperature of the BUS ( $T_B$ ) and the temperature of the ambient air ( $T_A$ ). Time in UT (2–24 hr).

Table III indicate that both antennas behave in a similar way. On the VertexRSI antenna, the invar cone shows a low thermal response, which together with the thermally stabilized focus cabin guarantees a stable base for the BUS. Using the data of Fig. 7 and Fig. 8, we are able to relate the path length variations  $\Delta L_1$  (pedestal) and  $\Delta L_2$  (fork) to the variation of the steel temperature ( $T_M$ ) and the ambient air temperature ( $T_A$ ). The corresponding values are given in Table IV.

TABLE III  
INSULATION EFFICIENCY  $\beta$  OF THE ANTENNA COMPONENTS

Antenna	Pedestal	Traverse	Fork (L/R)	Invar Cone	BUS
VertexRSI	0.14	0.20	0.24/0.26	0.06	0.72
AEC	0.13	0.22	0.22/0.14	–	–

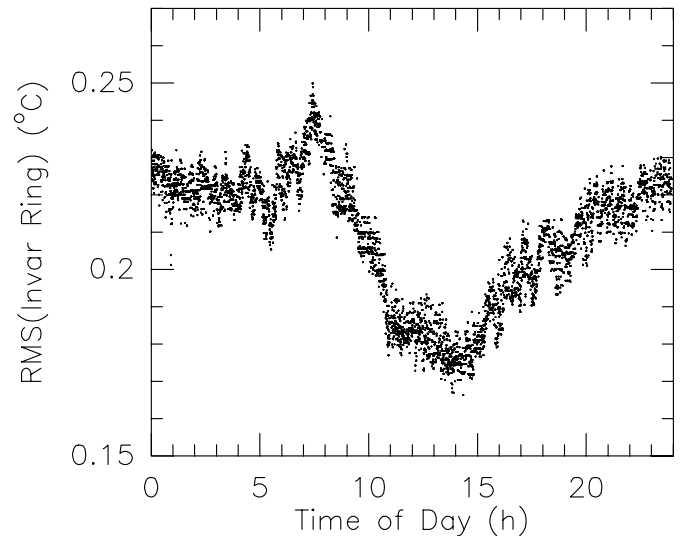


Fig. 25. VertexRSI antenna. The rms value of the temperature homogeneity of the invar ring supporting the BUS. Data from four consecutive days.

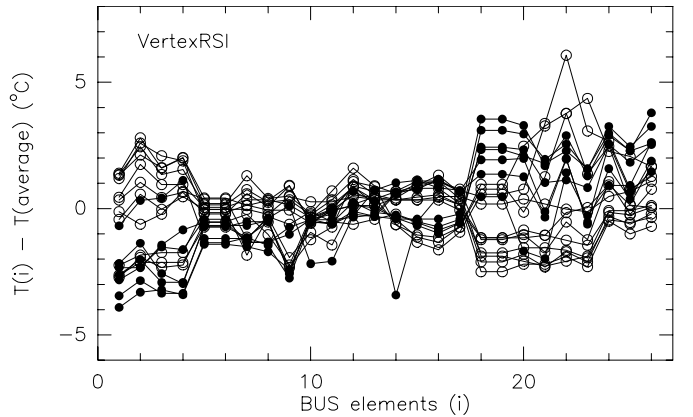


Fig. 26. VertexRSI antenna. Temperature distribution of the BUS for a stationary antenna (open circles) facing south, and the antenna tracking the Sun (dots). Shown are the temperature deviations of the 26 BUS elements with respect to the instantaneous average temperature of the BUS. Each line, is for a selected hour of the day.

### E. Thermal Tilt of the Elevation Axis

The sensors of each fork arm allow the determination of the differential thermal dilatation of the arms:

$$\delta L_2 = L \Delta T_l - L \Delta T_r. \quad (1)$$

This differential dilatation results in a change of the elevation axis tilt:

$$\Delta \epsilon = \frac{\delta L_2}{D} \quad (2)$$

in the direction of the axis. Although this tilt will be recovered, and corrected, in regular pointing observations, the magnitude  $\Delta \epsilon$  gives nevertheless an indication of the thermal stability of the fork. For the selected day, Fig. 27 shows the measured average temperature of the fork arms  $\langle T_f \rangle$ , with the width of the line indicating the value  $|T_f(l) - T_f(r)|$ , and the tilt  $\Delta \epsilon$ . There occurs a change in  $\Delta \epsilon$  with sunrise and sunset. The change, evaluated for approximately 14 days, is expected to be

TABLE IV  
PEDESTAL AND FORK ARM PATH LENGTH VARIATION (IN MM/° C)

Antenna	Pedestal $\partial L_1/\partial T_M$	Fork Arm $\partial L_2/\partial T_M$	Pedestal $\partial L_1/\partial T_A$	Fork Arm $\partial L_2/\partial T_A$
VertexRSI	0.10	0.03	0.15	0.0075
AEC	–	0.025	–	0.005

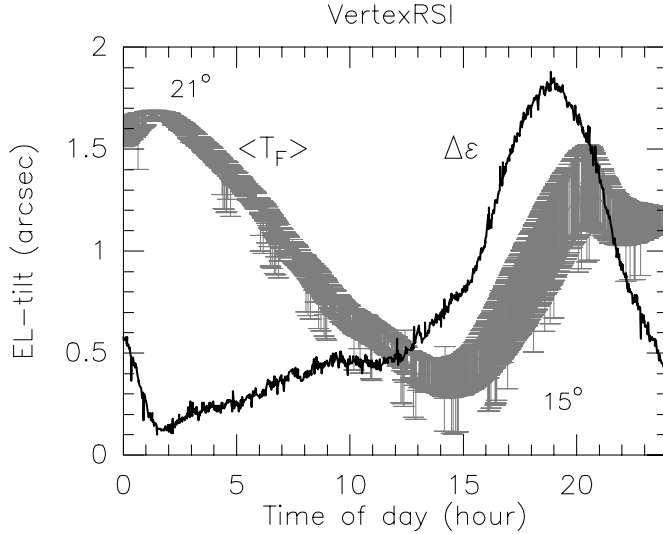


Fig. 27. VertexRSI antenna. Average temperature of the fork arms  $\langle T_f \rangle$  and temperature dispersion (width of the line). Predicted axis tilt  $\Delta\epsilon$ .

$\Delta\epsilon \lesssim 5''$  even if the antennas of the arrays track a target for a long time while asymmetrically illuminating the fork arm structure.

## VII. PRECISION OF THE AZIMUTH BEARING

### A. Measurements of the VertexRSI Antenna

The specification requires a 2-arcsecond (rms) blind pointing accuracy and a 0.6-arcsecond (rms) pointing accuracy for FSW observations in a field of 2° radius. For analysis of the antenna pointing and the understanding of the pointing model it is useful to know which part of the azimuth axis pointing error is due to the azimuth bearing. Accordingly, appropriate higher order terms of the azimuth angle  $A$  are introduced in the pointing model.

Measurements with the tiltmeter installed above the AZ bearing made at a slow speed (0.1°/s) and  $\pm 260^\circ$  rotation in AZ show, for both antennas, a single-angular sinusoidal response [ $\sin(A)$ ] to the inclination of the antenna (and foundation), and in addition a smaller three-angular sinusoidal response [ $\sin(3A)$ ] on the VertexRSI antenna, and an additional two-angular response [ $\sin(2A)$ ] on the AEC antenna. On the VertexRSI antenna, the three-angular wobble amounts to  $\pm 2$  arcsec; the extrema of the wobble are correlated with the position of the three-corner support of the pedestal, as shown in Fig. 28. This three-angular wobble is a print-through of the pedestal mount. After elimination of the components  $\sin(A)$  and  $\sin(3A)$ , the residual repeatable deviation is 0.5 arcsec rms. The best-fit values of the measurements to  $a_0 + a_1 \sin(A + b_1) + a_3 \sin(3A + b_3)$  are given in Table V. The residual curves  $b$  in Fig. 28 can be used in a lookup table for correction.

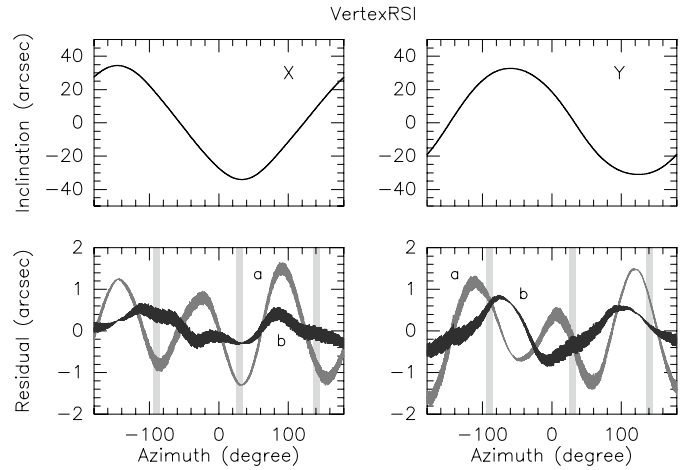


Fig. 28. VertexRSI antenna, measurement of  $-180^\circ$  to  $+180^\circ$  AZ rotation. The left panel is the x-direction of the tiltmeter, the right panel is the y-direction. The curves  $a$  are the residuals of the best-fit  $a_0 + a_1 \sin(A + b_1)$ , the curves  $b$  are the residuals of the best-fit  $a_0 + a_1 \sin(A + b_1) + a_3 \sin(3A + b_3)$ . The gray lines show the location of the pedestal corners (1,2,3) (from [2]).

TABLE V

VERTEXRSI ANTENNA: PARAMETERS OF THE AZ AXIS INCLINATION AND WOBBLE (IN BRACKETS VALUES REMEASURED AFTER ONE YEAR)

Linear	response	Linear	+ 3 A response
$a_0$	64.49 (53.08)''	$a_0$	64.47 (53.08)''
$a_1$	-68.41 (-65.02)''	$a_1$	-68.31 (-64.93)''
$b_1$	56.66 (59.77)°	$b_1$	56.811 (59.91)°
		$a_3$	-2.29 (-2.35)''
		$b_3$	-10.84 (-4.64)°
rms(residual)	1.69 (1.70)''	rms(residual)	0.60 (0.50)''

### B. Measurements of the AEC Antenna

The two-angular response [ $\sin(2A)$ ] on the AEC antenna, shown in Fig. 29 is attributed to an unevenness of the AZ bearing. This two-angular wobble amounts to  $\pm 1$  arcsec. After elimination of the components  $\sin(A)$  and  $\sin(2A)$ , the residual repeatable deviation is 0.7 arcsec (rms). The best-fit values to the measurement to  $a_0 + a_1 \sin(A + b_1) + a_2 \sin(2A + b_2)$  are given in Table VI.

The installation of an inclinometer on the center of the azimuth bearing allows an easy, and repeatable determination of the run-out or wobble of the azimuth bearing, which can be used in the pointing model as constant terms. This has been used on many telescopes (*cf.* [5]). The main advantage obtained with such an inclinometer on the azimuth bearing is that it allows an update of the pointing constants describing the

TABLE VI

AEC ANTENNA: PARAMETERS OF THE AZ AXIS INCLINATION AND WOBBLE

Linear	response	Linear	+ 2 A response
$a_0$	-2.65''	$a_0$	-2.66''
$a_1$	-10.71''	$a_1$	-10.75''
$b_1$	-81.21°	$b_1$	-81.47°
		$a_2$	0.98''
		$b_2$	39.13°
rms(residual)	0.99''	rms(residual)	0.73''

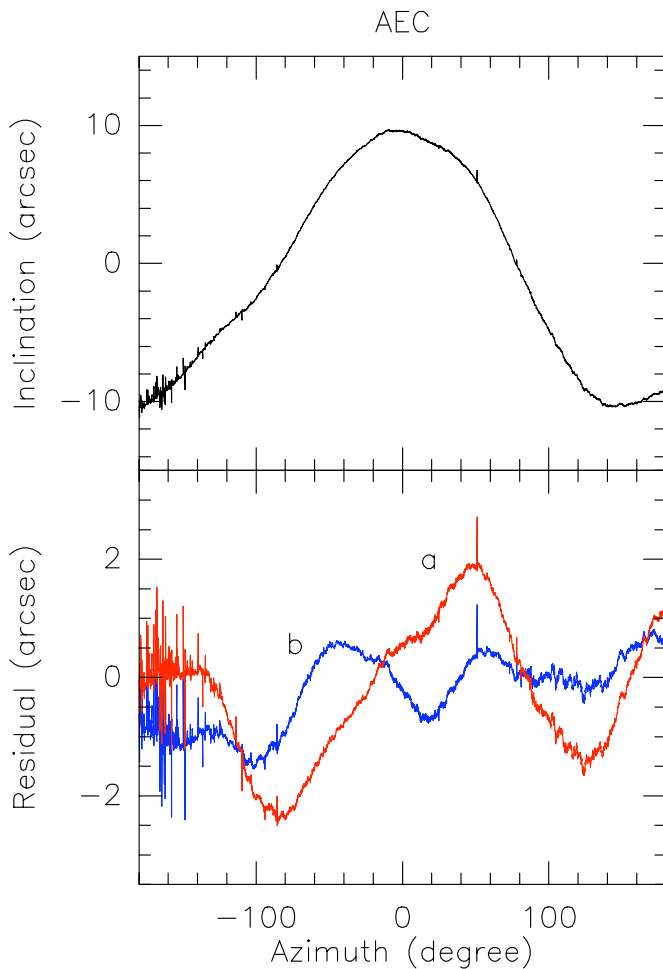


Fig. 29. AEC antenna measurements of  $-180^\circ$  to  $+180^\circ$  AZ rotation (top panel). The curve *a* (lower panel) are the residuals of the best-fit  $a_0 + a_1 \sin(A + b_1)$ , the curve *b* are the residuals of the best-fit  $a_0 + a_1 \sin(A + b_1) + a_2 \sin(2A + b_2)$ .

tilt of the AZ axis whenever the slew angle between sources is larger than  $\sim 60$  degrees ([6]).

### VIII. CONCLUSIONS

The measurements indicate that the path length specifications are fulfilled on both antennas, at least during time intervals of 1/2 to 1 hour. The path length variation is primarily due to unavoidable residual thermal dilatation of the (insulated) antenna steel components, and may span  $\sim 200 \mu\text{m}$  within a day. The path length variation can be predicted with high precision from temperature measurements at a few positions of the steel components, either used in empirical relations or the finite element model. It is expected that identical antennas will experience similar temperature variations of the ambient air so that the differential effect may even be smaller than stated here. Wind at speeds below the specification limit (9 m/s), and OTF and FSW motions of the antennas, do not degrade the path length stability.

As far as possible to measure, the antennas show similar behaviour of damping of the thermal environment, *i.e.* the ambient air temperature and the solar radiation. The BUS of

the VertexRSI antenna shows a good temperature homogeneity, even under full exposure to Sun shine.

Although the AZ bearings have a higher order azimuth dependent wobble, the effect can be considered in the pointing model with an accuracy better than 0.6 arcsecond. On the VertexRSI prototype antenna, the wobble was very stable with time.

### ACKNOWLEDGMENTS

The data were collected at the VLA site by A. Otárola (ESO & NRAO), N. Emerson and J. Cheng (both at NRAO, Tucson, USA). The measurement of the antenna when tracking the Sun was made by the Antenna Group (NRAO, Tucson, USA). The FEM data of the VertexRSI antenna were provided by Vertex-Germany (Mr. Omlor, November 2003) and are based on the original ASKA model. The FEM data of the AEC antenna were provided by Mr. Koch (ESO; April 2003) and are based on the model provided by EIE in March 2003. The comparison of temperature induced path length variations and FEM predictions are based on the FEM models of the antenna steel parts, provided by NRAO-Tucson and EIE-ESO, and used by M. Bremer (IRAM, France). Many data were extracted from the DataBase (F. Stauffer, NRAO, Socorro, USA).

### REFERENCES

- [1] R. Gušten, R. S. Booth, C. Cesarsky, K. M. Menten, "APEX - The Atacama Pathfinder EXperiment", *SPIE*, **6267**, p. 37
- [2] J. G. Mangum, J. W. M. Baars, A. Greve, R. Lucas, R. C. Snel, P. T. Wallace, and M. Holdaway, "Evaluation of the ALMA Prototype Antennas", *PASP*, **118**, 2006, pp. 1257-1301
- [3] R. Ambrosini, G. Grueff, M. Mrsiani, G. Maccaferri, P. Zacchiorli, and A. Orfei, "Analysis of the Alidade Temperature Behaviour of the Medicina VLBI Radiotelescope", *Astroph. and Space Sci.*, **239**, 1996, pp. 247-258
- [4] M. Bremer, and J. Peñalver, "FE Model Based Interpretation of Telescope Temperature Variations", *Proc. SPIE*, **4757**, 2002, p. 186
- [5] W. Gawronski, F. Baher, and O. Quintero, "Azimuth-Track Level Compensation to Reduce Blind-Pointing Errors of the Deep Space Network Antennas", *IEEE Ant. Propagat. Magazine*, **42**, 2000, p. 28
- [6] J. Penalver, U. Lisenfeld, and R. Mauersberger, "Pointing with the IRAM 30-m Telescope", *SPIE*, **4015**, 2001, p. 632

PLACE  
PHOTO  
HERE

**Albert Greve** was born in Germany. He studied astronomy at Leiden University, Leiden, The Netherlands and received the Ph.D. degree from Utrecht University, Utrecht, The Netherlands, in 1978.

He worked at Culhan Laboratory, UK, the Queens University, Belfast, Ireland, the Max Planck Institute for Radioastronomy, Germany, and at Institut de Radio Astronomie Millimétrique (IRAM), France and Spain. He was involved in the construction and testing of several radio telescopes, in particular surface adjustments and radio optics, but also in the thermal design of modern millimeter wavelength telescopes (and several optical telescopes). He worked in the field of radio astronomy, in particular mm-wavelength VLBI. He retired at the end of 2003.

Institut de Radio Astronomie Millimétrique, 300 rue de la Piscine, Domaine Universitaire, 38406 Saint Martin d'Hères, France (greve@iram.fr)

PLACE  
PHOTO  
HERE

**Jeffrey G. Mangum** received the Ph.D. degree in astronomy from the University of Virginia in 1990.

Following a two-year residency as a postdoctoral researcher in the astronomy department at the University of Texas he joined the staff of the Submillimeter Telescope Observatory (SMT) at the University of Arizona. In 1995 he joined the scientific staff at the National Radio Astronomy Observatory (NRAO) in Tucson, Arizona, and subsequently moved to the NRAO headquarters in Charlottesville, Virginia. His research interests include the astrophysics of star formation, the solar system, and external galaxies, the performance characterization of reflector antennas, and calibration of millimeter-wavelength astronomical measurements.

National Radio Astronomy Observatory, 520 Edgemont Road, Charlottesville, VA 22903, USA (jmangum@nrao.edu)